

Dissimilar Laser Joining of NiTi SMA and MP35N Wires

BOYD PANTON, ANDREW PEQUEGNAT, and Y. NORMAN ZHOU

The laser welding of NiTi alloy wire to MP35N wire was investigated to improve the understanding of dissimilar materials joining of NiTi shape memory alloys (SMAs), facilitating their future application in novel devices. Both positioning of the laser beam with respect to the joint's centerline and laser peak power were found to be critical variables affecting the physical and thermomechanical properties of the welded joint. Positioning of the laser beam was used to control the weld pool composition, while the laser beam intensity affected the pool size and mixing. These variables were shown to greatly affect hardness and susceptibility to cracking in the fusion zone, which heavily impacted the weld strength. With a lower peak power and the laser positioned over the MP35N wire, butt-welded wire joints were achieved with the ultimate load of 66 pct of the NiTi wire breaking load.

DOI: 10.1007/s11661-014-2280-7

© The Minerals, Metals & Materials Society and ASM International 2014

I. INTRODUCTION

THE unique properties of NiTi shape memory alloys (SMAs) have led to their considerations in an increasing number of engineering designs in a variety of industries ranging from aerospace to medical.^[1–3] Integration of NiTi SMAs into these diverse fields is desirable in order to utilize the shape memory effect (SME), pseudoelasticity (PE), and biocompatibility properties for developing novel devices. For example, PE has been exploited for several decades in novel medical device applications such as PE wire and tubing for angioplasty procedures, stents, and orthodontic arch wires.^[3,4] Recent advances in key technologies have facilitated the application of the SME which enables novel actuation applications that can replace electromechanical systems, or achieve previously unattainable actuation in the micro and nanoscales.^[5–8]

Successful adoption of NiTi SMAs in engineering designs requires metallurgical joining, where current mechanical joining techniques are unfavorable or even impossible.^[8] There are a number of joining methods that have been investigated for use with NiTi alloys, which include resistance, friction, and laser welding processes.^[9–11] Pulsed Nd:YAG laser welding was exclusively investigated in the current study as it is one of the more promising joining methods, capable of achieving up to 80 pct joint efficiency.^[12–14]

There are several challenges in the joining of NiTi SMAs. Ti-rich alloys are prone to solidification cracking during laser welding due to a large freezing range and

formation of brittle Ti₂Ni phase at the grain boundaries of resolidified material.^[8,15,16] These joints exhibit a reduction in the elongation and the ultimate tensile strength (UTS), resulting in a brittle-type fracture.^[15,17] Furthermore, SMA properties are extremely sensitive to their chemical composition and previous thermomechanical processing history. These unique properties become altered or destroyed during joining processes.^[8,18–20]

Dissimilar material joining of NiTi alloys further complicates the welding process. There is significant change in SMA properties from the heat input into the base metal (BM) and composition alteration of NiTi in the dissimilar fusion zone (FZ).^[8,13,21] For example, laser joining of NiTi sheets with Cu and Ni interlayers reduces the local transformation temperature with respect to the BM.^[21] Similarly, the addition of Co, Cr, and Mo to the NiTi system has been found to suppress martensite transformation, but there has been no investigation of their effects on transformation temperatures in dissimilar joints.^[20,22] Brittle intermetallic formation also commonly occurs in NiTi dissimilar joints.^[10,16,23–26] These brittle phases have limited ductility and can crack due to the thermal stresses experienced during cooling.^[27–29] Ni and Co interlayers of optimal thicknesses (*i.e.*, 50 μm) have been utilized to suppress detrimental intermetallic formation in laser and friction dissimilar NiTi-SS joints.^[10,16,23–25] However, the use of interlayers complicates welding setups. Positioning of dissimilar materials with respect to the laser beam has been identified as a method for controlling the relative melting of the dissimilar materials, thus minimizing mixing and detrimental defects in the FZ.^[16,30,31] If the joint's geometry is restricted, then the laser can be offset with respect to the joint's centerline to control the FZ composition, restricting the formation of brittle intermetallics and/or other detrimental defects.^[27–29]

In dissimilar materials joining of NiTi SMAs, excessive brittle intermetallic formation must be avoided, and

BOYD PANTON and ANDREW PEQUEGNAT, Ph.D. Candidates, and Y. NORMAN ZHOU, Professor, are with the Centre for Advanced Materials Joining (CAMJ), University of Waterloo, 200 University Avenue West, Waterloo, ON N2L 3G1, Canada, and also with the Centre for Bioengineering and Biotechnology (CBB), University of Waterloo, 200 University Avenue West, Waterloo, ON N2L 3G1, Canada. Contact e-mail: bepanton@uwaterloo.ca

Manuscript submitted August 14, 2013.

Article published online April 15, 2014

the heat input into the NiTi SMA must be limited to prevent degradation of the mechanical and functional properties. Alloying in the FZ resulting from dissimilar joining greatly affects the phase transformation characteristics and hence, functional the properties of the SMA. Using this knowledge, a pulsed Nd:YAG laser process was developed to join NiTi SMA wire to MP35N (*i.e.*, Ni-Co-Cr-Mo alloy) wire. The objective of this investigation was to conduct a systematic study on the effects of peak power and joint centerline offset on the mechanical, metallurgical, and phase transformation characteristics.

II. EXPERIMENTAL METHODS

A. Materials

There were two materials used in the current study. The first was a 380- μm -diameter near-equiatomic Ti-rich NiTi Flexinol™ wire purchased from Dynalloy Inc. The wire has undergone a proprietary cold work and heat-treatment schedule and is reported to have a 363 K (90 °C) austenite start (A_s) transformation temperature. The second material was a 600- μm MP35N wire purchased from Alloy Wire International Inc., and Table I contains the reported composition. After being cold drawn, the wire was subject to an annealing treatment.

Before laser welding, the NiTi wire was cleaned with a 15 vol pct HF, 45 vol pct HNO₃, and bal. H₂O mixture, to remove the thick oxide layer. This is required for successful welds and led to a final average wire diameter of 340 μm .^[13]

B. Laser Welding

A Miyachi Unitek LW50A pulsed Nd:YAG laser system, with wavelength of 1.064 μm , a spot size of 400 μm , and a top hat-type spatial profile was used for laser welding. During welding, argon shielding gas with a flow rate of 0.51 m³ h⁻¹ (18 CFH) was used to avoid detrimental oxidation. A pulse profile of 3.5 ms including a 1-ms upslope and downslope was used with spots overlapped by 50 pct, and a 2-second wait time in between each laser spot. The short pulse width was designed to limit heat input into the HAZ and to limit mixing in the FZ. The peak powers were set at 0.5 and 0.7 kW to vary the weld pool size, degree of mixing, and ablation in addition to other possible effects. The positionings of the focused laser spot were varied: ± 100 μm (-100 μm = NiTi offset, 0 μm = Centered, and 100 μm = MP35N offset) from the centerline of the weld to alter the composition of the FZ. These processes were investigated to determine their effects on the joint's mechanical and functional performance. During welding, the wires were held securely together in a fixture

Table I. MP35N Chemical Composition (At. Pct)

Ni	Co	Cr	Mo	Other
34.9	34.3	19.8	9.73	0.9

(Figure 1) designed to counteract the SME effect that would be activated by the heat of the welding process.^[9]

The top of each of the wires was held at a common plane in order to promote wetting between the two wires and coalescence of the weld pools. Figure 2 contains a representative joint produced with 0.5 kW peak power and 100 μm offset into the MP35N wire.

C. Mechanical Testing and Microstructural Analysis

Tensile testing was performed at room temperature [approximately 292 K (19 °C)] using an Instron model 5548 microtensile tester with ± 0.5 - μm measurement accuracy. Three test samples were prepared for each set of parameters with a weld length of 7.5 mm and an overall gauge length of 50 mm. The weld was positioned equidistant between the pneumatic grips. The joints were tested under an ASTM F2516-07 protocol at a rate of 0.8 mm/min and were pulled to failure.

The peak load was measured from the tensile curves as the maximum load achieved during the tensile test. The joints failed in a number of ways including fracture along the length of the joint, during which time, the force was sustained or even increased. The effective joint area was ill defined in this case. To avoid reporting erroneous values, the measurement of load, but not stress, was reported in this investigation. The existence of the two base materials and the weld in the gauge length of the specimen result in the strain having little value in analysis. The strain will be a combination of elastic and plastic deformations of each of these regions overlapping one another and have no discernible use. Only the peak load achieved and the fracture mode can be obtained from this work due to the discontinuity in properties across the dissimilar materials and weld contained in the gauge length.

A micro-Vickers hardness tester (Shimadzu Corporation, Kyoto, Japan) was used to make a series of 50 g indents across the weld pool 30 μm apart with a hold time of 20 seconds. Samples were etched with 7.5 (vol pct) mL HF, 20 (vol pct) mL HNO₃, and bal. H₂O

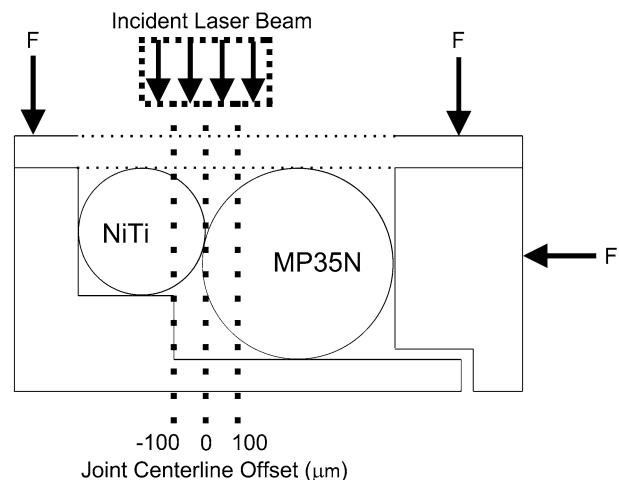


Fig. 1—Schematic of wire configuration during fixturing for laser welding (not to scale).

solution for a duration ranging from 12 to 15 seconds to reveal the microstructure. The microstructure was observed using an Olympus BX51M optical microscope system. EDX analysis was performed using an INCA energy 350 EDX microanalysis system equipped with a JEOL JSM-6460 SEM using an acceleration voltage of 20 kV. A Zeiss Leo 1550 Field Emission SEM with an accelerating voltage of 10 kV was used for observation of the submicron cracks and surrounding microstructure.

D. Thermoanalytic Analysis

Phase transformation temperatures of the various joints were identified using a Thermal Analysis Q2000

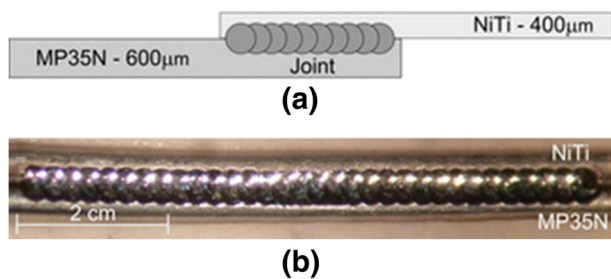


Fig. 2—Wire butt joint configuration (a) schematic (not to scale), and (b) example weld.

differential scanning calorimeter (DSC) equipped with a refrigerated cooling unit. A modified ASTM F2004-05 standard test method was used for these tests, with modifications consisting of test temperatures ranging from 198 K to 393 K ($-75\text{ }^{\circ}\text{C}$ to $120\text{ }^{\circ}\text{C}$) and a test rate of $5\text{ }^{\circ}\text{C}/\text{min}$. The start and finish transformation temperatures—*austenite start* (A_s), *austenite finish* (A_f), *martensite start* (M_s), and *martensite finish* (M_f)—were determined by taking the intercept of the tangents to the phase transformation peak and base line, as per the ASTM standard. The specimens used during the DSC analysis were the entire cross sections of both BMs and the FZ.

III. RESULTS AND DISCUSSION

A. Microstructural, Compositional, and Hardness Analyses

Figure 3 displays the optical images of the dissimilar joint cross sections. Etching revealed the flow and mixing of the two alloys in the FZs of the joints. Figure 3 also indicates the path of the EDX compositional analysis (Figure 4), which was performed across the joints. The EDX analysis showed an increase in MP35N alloying elements (*i.e.*, Co, Cr, Mo) and a decrease in the Ti composition as the scan progressed across the FZ from the NiTi BM toward the MP35N BM. Inhomogeneity across the FZ is well documented in

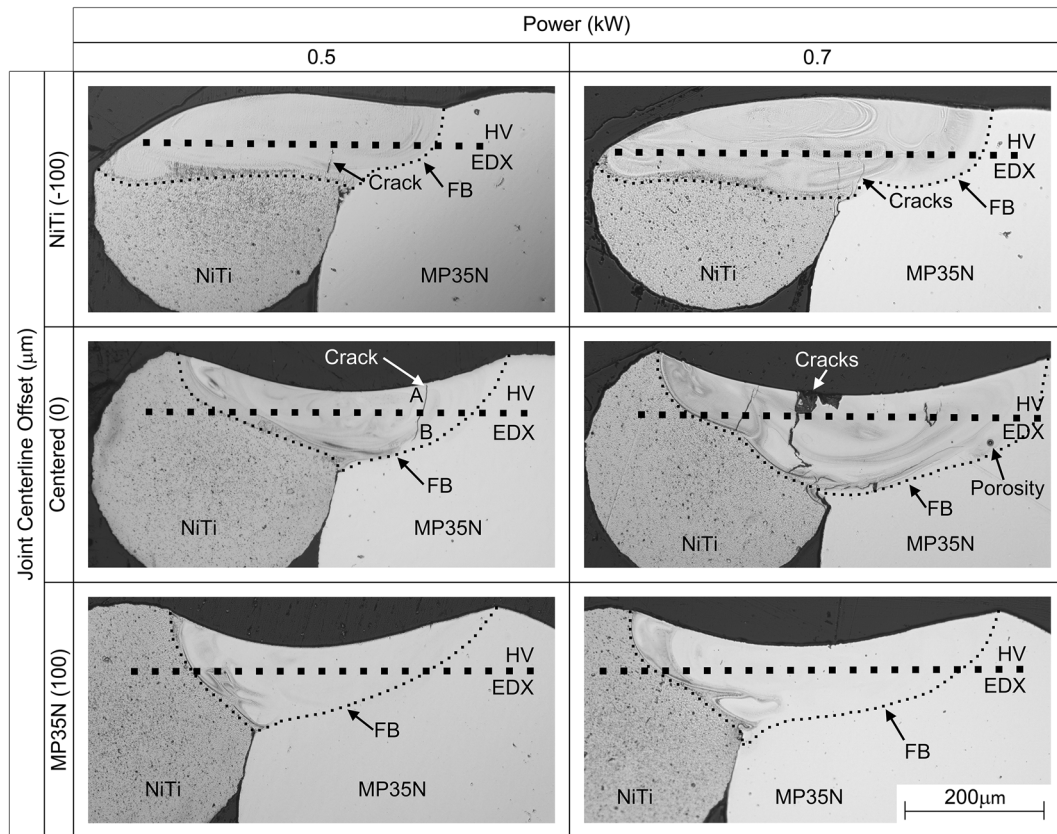


Fig. 3—0.5 kW and 0.7 kW peak powers in joint cross sections with EDX scan and microhardness (HV) test locations indicated.

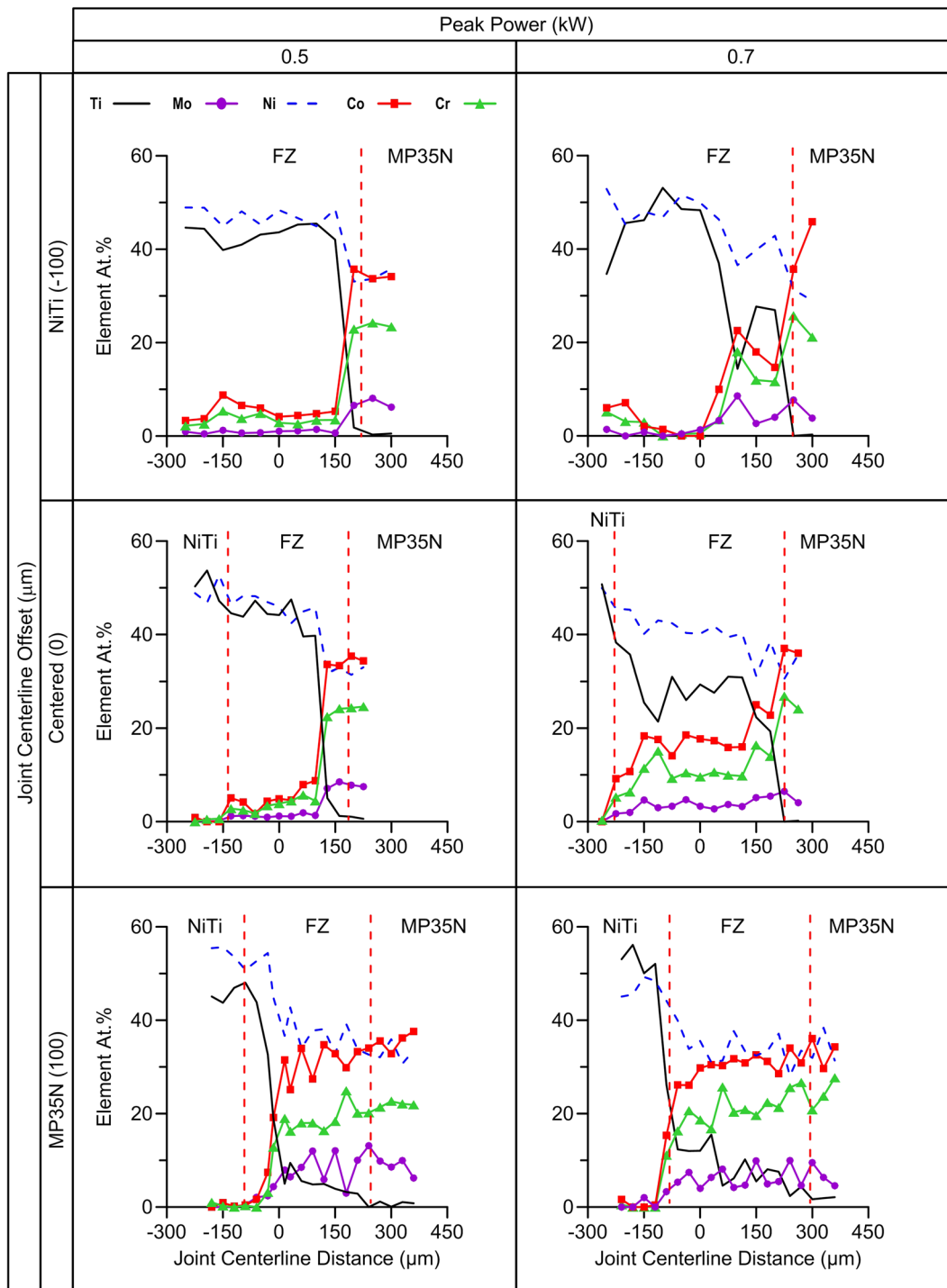


Fig. 4—Elemental composition measured across joint cross sections.

the joining of NiTi to dissimilar materials.^[23,24] The inhomogeneity was caused by variations in the marangoni forces and flow in the weld pool that results from both the high-heating and -cooling rates present in laser welds, and the addition of dissimilar alloying elements.^[28,32] The EDX analysis showed that the increasing the peak pulse power increased the mixing of Ti with the MP35N elements in the FZ. This increase in homogeneity of the FZ with greater power input has

been previously related to greater weld pool flow and greater BM dilution.^[16,33,34] Offsetting the laser into either BM resulted in a FZ composition dominated by the alloy into which the laser was offset. Focusing the laser on the joint's centerline (*i.e.*, 0 μm offset) increased mixing of Ti with the MP35N alloying elements. The presence of large amount of intermetallic oxides is typical of Ti-rich NiTi BM.^[35] These Ti-rich oxides are seen as the dark spots in the NiTi BM and measure

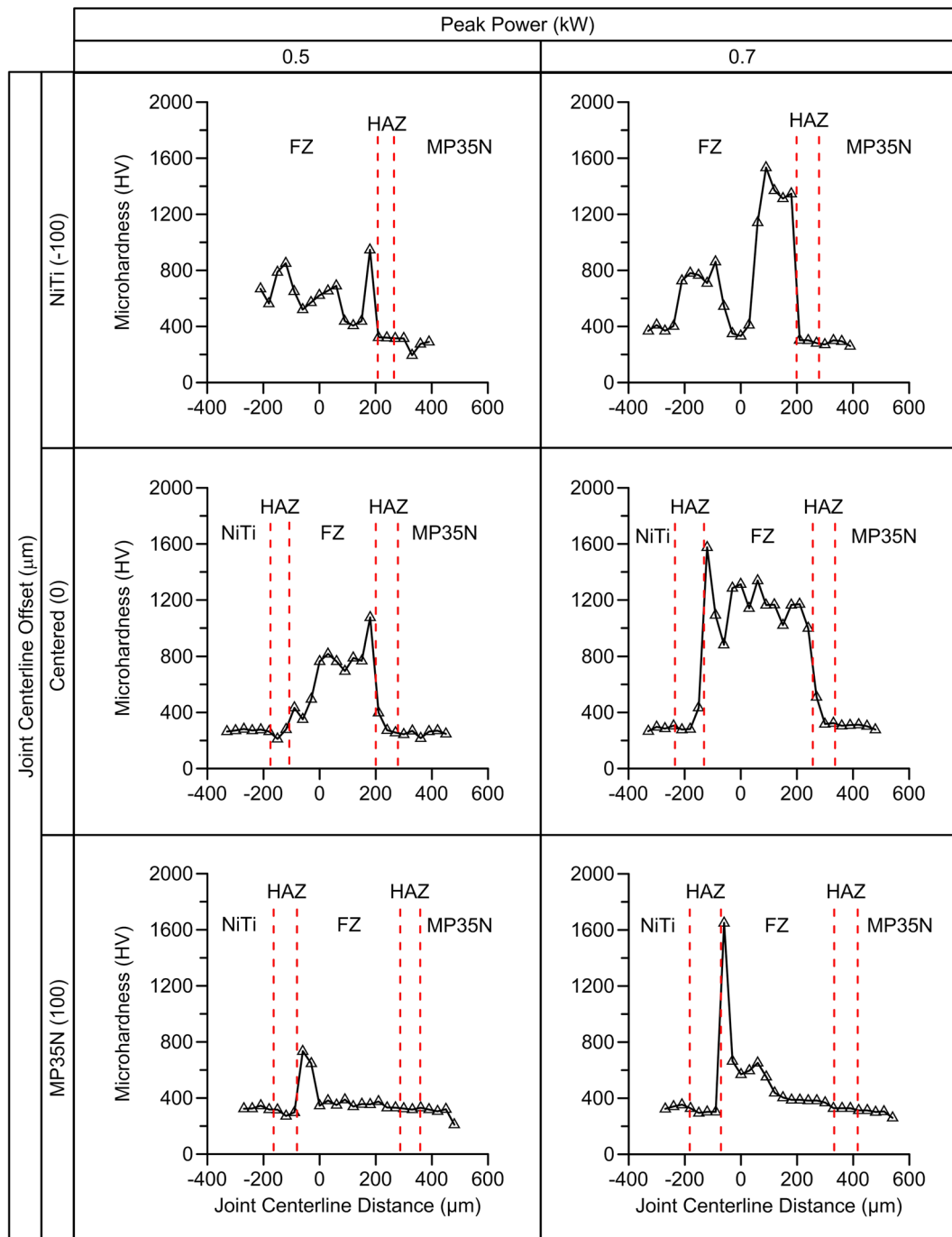


Fig. 5—Microhardness values measured across joint cross sections (see Fig. 3).

$0.7 \pm 0.5 \mu\text{m}$, having an area fraction of 4 pct. The presence of these intermetallics may affect the compositional analysis of the NiTi BM.

Hardness profiles presented in Figure 5 were taken near the EDX scan lines (Figure 3). Higher peak power resulted in a slightly greater HAZ width and softening of the NiTi wire, which had undergone a proprietary cold drawing and heat-treatment process. There was no appreciable softening of the MP35N wire because it was previously annealed by the manufacturer. The hardness

of the FZ was on average higher than the BM. The regions that had the highest hardness values were the regions that had the greatest mixing of Ti with the MP35N alloying elements.^[16,25] The higher hardness of the FZ was due in part to solid solution strengthening resulting from the mixing of the MP35N elements with NiTi.^[35] High hardness values in the FZ have also been shown to be caused by the formation of brittle Ti intermetallics (Ti_2Ni , Ti_2Co , TiCr_2 , *etc.*) that can occur in Ti-rich and dissimilar NiTi joints.^[10,15,16,23–25,36] The

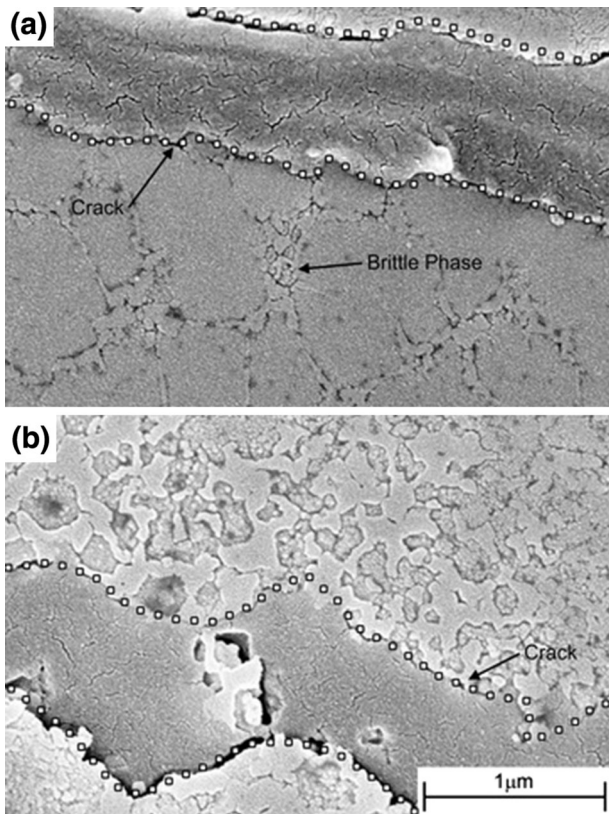


Fig. 6—Magnified regions of the 0.5 kW, centered specimen from Fig. 3. Along the crack observed in this specimen was a gradient of mixing which was accompanied by a variation in the microstructure as seen in (a) the region dominated by NiTi, and (b) the region with mixing of NiTi and MP35N.

formation of these brittle intermetallics depends on the amount of mixing between the Ti and MP35N elements. Areas of intense mixing coincided with peaks in the hardness values which suggests the formation of brittle intermetallics.^[27,28] Higher peak powers led to greater mixing and resulted in higher hardness values in the FZ. Offsetting the laser into the BM led to a hardness profile that decreased across the FZ, which correlated with the decrease in mixing of Ti into the FZ. The NiTi offset specimen had a much higher hardness on average than the MP35N specimen from the formation of brittle Ti_2Ni intermetallics, which is known to occur in Ti-rich FZs.^[15] Focusing the laser on the joint's centerline led to a much more even hardness across the FZ, consistent with the more even mixing in these joints (*i.e.*, more homogeneous formation of brittle intermetallics).

Regions of greater mixing in the FZ were accompanied by more cracking as previously identified in the optical microscopy analysis of Figure 3. Many of the cracks formed near the triple point where the two BMs and the FZ meet. The incomplete penetration present at this point locally increased the stress and was a result of the partial penetration weld design that was used to limit both the mixing of the alloys and the alteration of the NiTi BM properties. Cracking in dissimilar NiTi joints has been attributed to both solidification cracking, and the failure of brittle intermetallics that are subjected to

the thermal stresses that occur during cooling.^[16,23–25,27–29] The 0.5 kW, centered specimen contained a long crack (Figure 3) that traversed regions that had experienced different intensities of mixing. Figure 6(a) shows a section of the crack in a region dominated by NiTi. The crack did not contain any solidified dendritic surfaces typical of solidification cracking, but instead the crack's surface was covered in microcracks. The microstructure surrounding the crack was composed of equiaxed dendrites surrounded by a brittle phase that had experienced excessive cracking. This brittle microstructure in the FZ is inherent to Ti-rich NiTi welds.^[8,15,16] In the intensely mixed region seen in Figure 6(b), the crack's surface was again covered in microcracks. The mixing that occurred in this region resulted in a complex equiaxed microstructure through which the brittle crack propagated. Previous investigations linked the formation of fine equiaxed grains to the undercooling which resulted from the high-cooling rates of laser welding and the inhomogeneity of the composition in the FZ.^[37] The small size of these grains has been shown to impede solidification cracking.^[28] The lack of evidence for solidification cracking and the brittle cracked features of the microstructure indicate that the macrocracks occurred due to the failure of brittle intermetallics during cooling of the FZ. The most intense cracking occurred in the 0.7 kW, centered joint. This joint had experienced the greatest mixing and had the highest, most uniform hardness profile across the FZ. This led to the highest potential for brittle intermetallic formation and resultant cracking of these phases in addition to other defects such as the porosity (Figure 3).^[16,23–25] Therefore, it can be stated that decreasing the laser power decreased the amount of cracking in all joints. Offsetting the laser into either BM reduced mixing in the FZ and also led to reduced cracking, whereas no cracking was seen in the MP35N offset joint. The EDX scans of the MP35N offset joints revealed that the majority of the FZ was Ni and Co rich, but not Ti rich. The risk of crack formation in these joints was reduced due to the lower brittle intermetallic content, implicit by the lower hardness profile.^[25] Furthermore, Ni and Co-rich intermetallics are less susceptible to cracking as they are more ductile than the Ti-rich intermetallics.^[16] The weld pool size, heat input, and cooling rate should also be taken into consideration when analyzing joint defects; however, they have been shown to be subordinate to the effects of mixing in the weld pool.^[28]

B. Mechanical Performance and Fractography

Figure 7 illustrates the fracture paths that resulted from the variation in welding parameters. The fracture surfaces of the low and high-powered specimens were very similar, and so only the 0.7 kW specimen fracture surfaces are shown in Figures 8, 9, and 10.

Figure 11 gives the peak load obtained from the tensile tests of the specimens, plotted against peak power and joint offset. The substantial variation in the peak load results from a number of factors, including variation in joint cross-sectional area and the occurrence

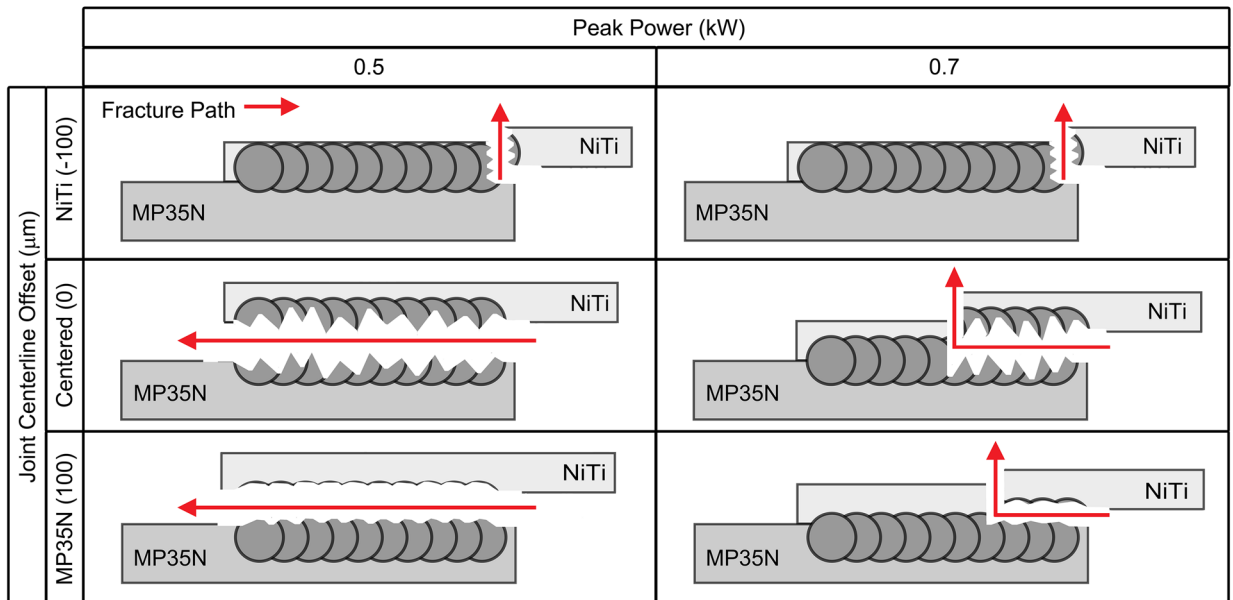


Fig. 7—Schematic of fracture path dependence on welding parameters.

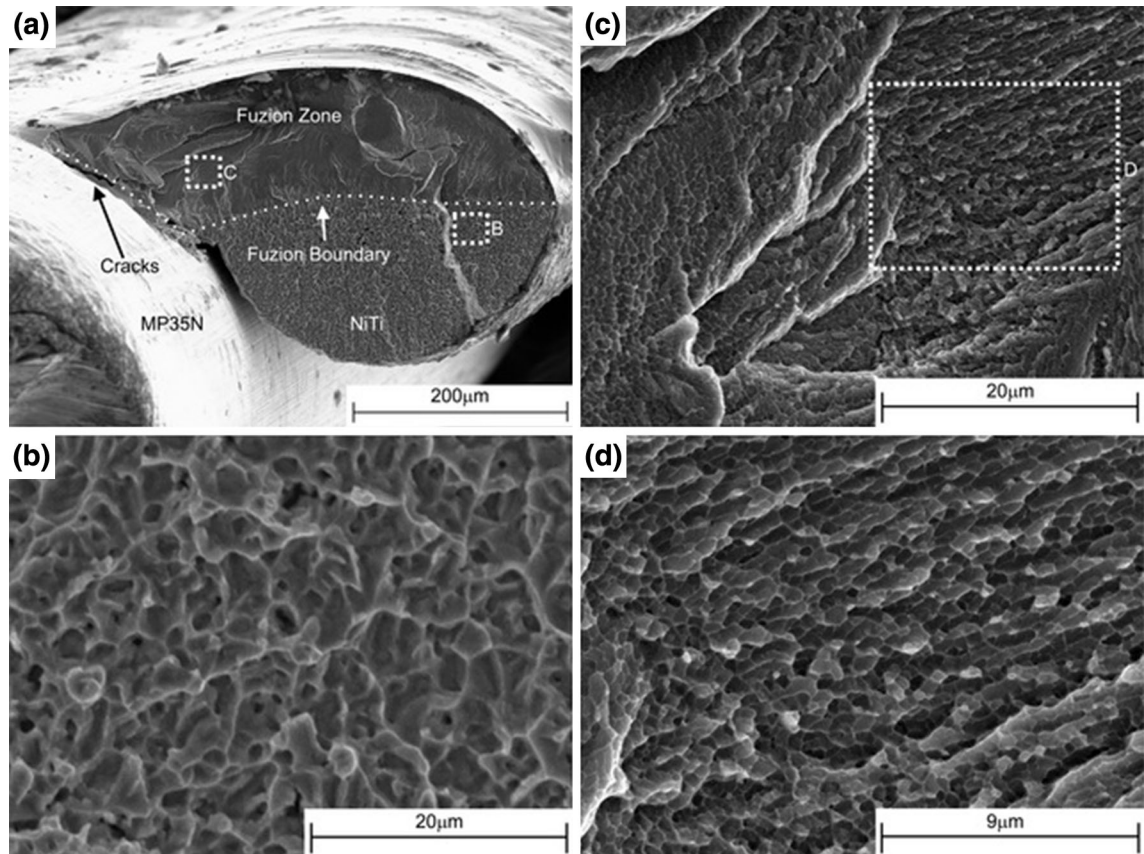


Fig. 8—(a) 0.7 kW, NiTi (-100 μm) offset fracture specimen; (b) ductile fracture in BM; (c) Brittle interdendritic fracture in FZ; and (d) Magnified section of (c), highlighting brittle fracture surface with uniform direction.

of defects in the joints. These differences will be discussed in detail later.

Failure in the NiTi offset specimens as depicted in Figure 7 occurred at the first pulse of the joint.

Figure 8(a) shows that the failure occurred through both the FZ and the BM/HAZ of the NiTi wire. Figure 8(b) shows that ductile fracture occurred in the BM, and Figure 8(c) shows that brittle interdendritic

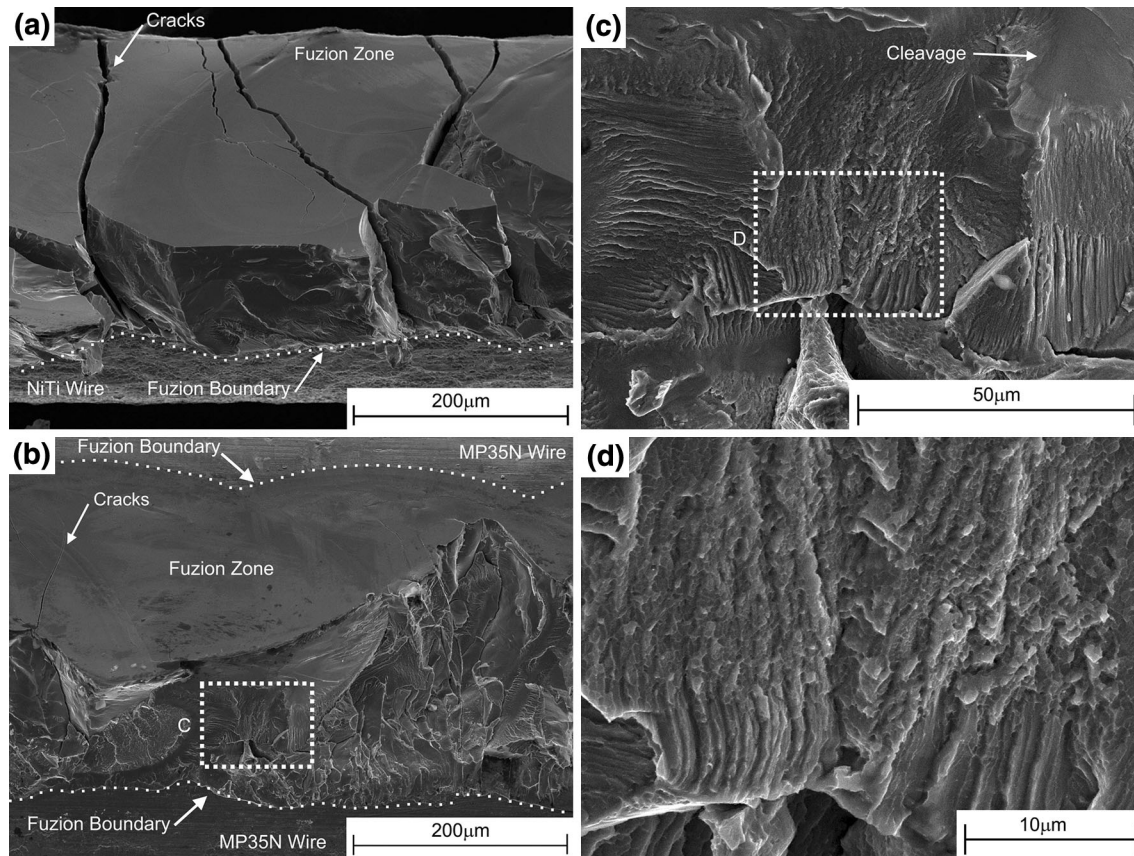


Fig. 9—0.7 kW, centered (0 μm) offset fracture specimen: (a) NiTi wire side of FZ; (b) MP35N Wire side of FZ; (c) fracture surface containing brittle interdendritic fracture and some cleavages (top right) fracture; and (d) magnified section of (c), highlighting brittle interdendritic fracture.

fracture occurred in the FZ. The composition of the FZ of these joints was dominated by the NiTi wire (Figure 4), which was Ti rich. The brittle fracture through the FZ is typical of dissimilar or Ti-rich NiTi welds that have been weakened by the formation of brittle Ti intermetallics.^[15,23,24] There was no evidence of solidification cracking (*i.e.*, dendrites) on the fracture surfaces of these joints, suggesting that the cracking observed in the cross sections was due to failure of brittle intermetallics from thermal stresses experienced during the cooling of the FZ.^[27–29] Cracking can be seen along the FZ-MP35N interface on the fracture surface (Figure 8(a)) indicating this region along with the triple point as possible regions for failure initiation. Failure has previously been shown to occur at the interface between the BM and FZ due to a combination of the discontinuity in mechanical properties at the interface, the stress concentrations from the weld profiles (and the triple point in this case), and other defects including cracks.^[26] The large brittle FZ was cracked but had sufficient area to bear the load. The softened NiTi BM had insufficient area to bear the load, and so fracture occurred across the BM/HAZ as seen in Figures 7 and 8(a), and not along the length of the joint through the brittle FZ. Fracture through the reduced NiTi BM area was the cause of the NiTi offset joints having the lowest peak loads.

In the centered specimens, brittle failure occurred through the length of the FZ (Figures 9(a) and (b)),

along the length of the joint (Figure 7). Much more cracking was observed in the NiTi half of the fracture specimen (Figure 9(a)). The brittle cracking of this half of the FZ suggested greater brittle intermetallic formation in this region, which was expected due to the higher hardness values, and the greater mixing of Ti into the FZ. Similar to the NiTi offset specimen there was significant interdendritic fracture (Figure 9(d)); however, there were also smaller areas of brittle cleavage throughout the fracture surface (Figure 9(c)). The cross sections of the centered joints contained excessive cracking; however, there was no evidence of solidification cracking on the fracture surfaces. Material was observed to fall from the joint during tensile failure, which could have removed evidence of solidification cracking from the fracture surfaces of the specimens. Previous studies have attributed similar cracking as was observed in the cross sections to fracture of brittle intermetallics during cooling of the FZ.^[27–29] Failure initiated from the extensive cracking in the FZ, and was aided by the triple-point defect as failure propagated along the length of the weld. The area of the NiTi BM was sufficient to sustain loading and not fail during propagation of this fracture. The FZ had been weakened by the cracking, and so the peak load was not substantially higher than the NiTi offset specimens.

Figure 7 shows that the MP35N offset joints experienced brittle failure along the NiTi-FZ interface. Figure 10(a) shows the resultant weld nugget pull-out

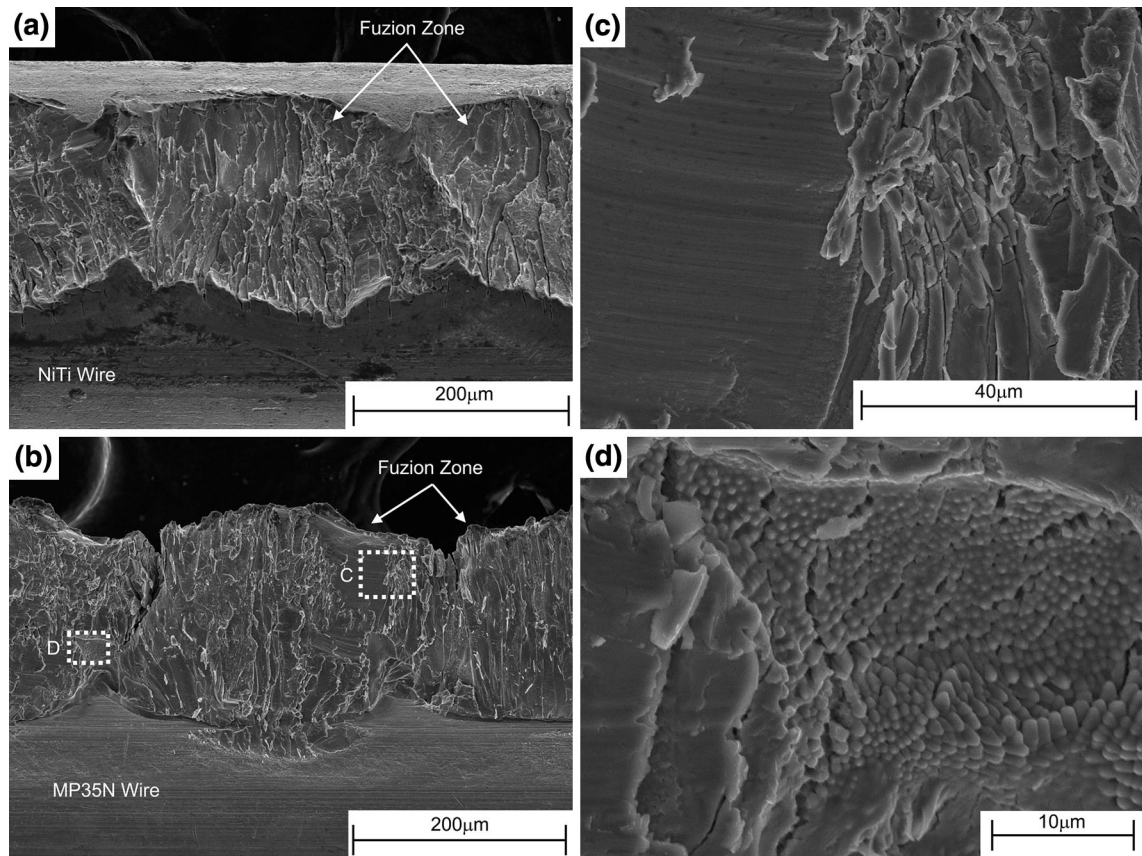


Fig. 10—0.7 kW, MP35N (100 μm) offset fracture specimen: (a) NiTi wire showing FZ nugget pullout, (b) MP35N wire with FZ attached, (c) brittle cleavage typical of majority of surface, and (d) solidification cracking found in a minority of regions.

from the NiTi wire, and Figure 10(b) shows the FZ attached to the MP35N wire. Previous investigations attributed a similar failure mode to the concentration of brittle intermetallics near the FZ-BM interface.^[25,28] At the NiTi-FZ interface, there was an increased concentration of Ti (Figure 4) and an isolated peak in hardness (Figure 5), indicating an isolated area of brittle intermetallic formation.^[27,28] Figure 10(c) shows brittle cleavage fracture which was observed over the majority of the fracture surface. Some solidification cracking was observed in isolated regions (Figure 10(d)), which led to weakening of the interface in addition to providing failure initiation points. The small sizes of these solidification cracks impeded their detection in the cross sections (Figure 3). The major defects in these joints were isolated to the NiTi-FZ interface, leading to failure in this region. The area of the NiTi BM was sufficient to bear the load, while failure propagated through the FZ along the NiTi-FZ interface. Crack initiation began at this highly stressed brittle interface, potentially at the triple point defect, and propagated along the interface for the length of the weld.^[10,25,26] The curved surface of the laser spots impeded the crack propagation; during tensile testing, the failure was arrested as it progressed along the interface during which time, the peak load increased. This was a much slower failure than the centered specimens that broke very rapidly. These joints attained a much higher load than the other joints due to

the lower amount of defects isolated to a restricted region of the FZ. Maximum peak loads of 92 ± 4 N were achieved by the 0.5 kW, MP35N offset joints. The maximum peak load was therefore 66 pct of the 140 ± 1 N breaking load of the NiTi alloy.

Some of the 0.7 kW, centered and MP35N offset specimens failed through the NiTi BM as shown in Figure 7, while others failed through the FZ like their respective 0.5 kW counterparts. A number of factors contributed to this change in failure mode with increase in power, including the increase in weld pool size (reduction in NiTi BM cross-sectional area), HAZ softening, and potential experimental error in offset positioning.

C. Phase Transformation Characteristics

The functional properties of the SMA wire and joint are important in SMA actuation applications. Dissimilar joining of these materials may significantly alter the functional properties. Thorough analysis of these new properties was necessary to determine if any changes induced during welding will affect the device performance in application. Differential scanning calorimetry analysis presented in Figure 12 shows the changes in the phase transformation characteristics of the joints and therefore functional properties of the weld material. Analysis of the BM in the as-received (AR) and

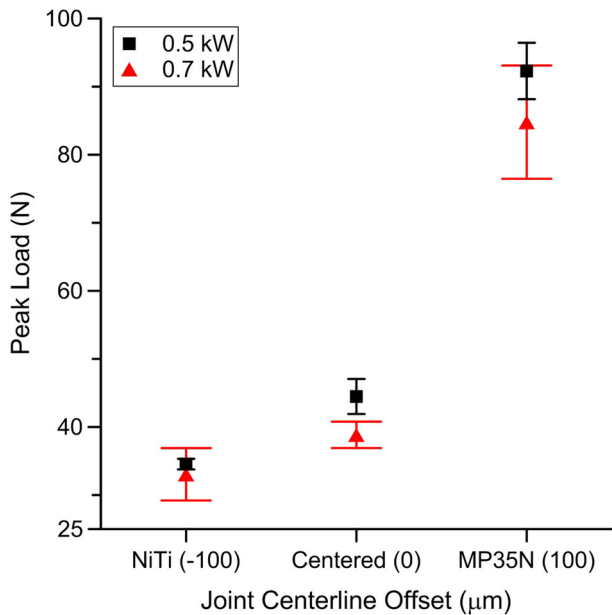


Fig. 11—Effects of joint centerline offset and power on the peak load. Error bars represent one standard deviation. Inconsistent joint area and defects contribute significantly to interparameter variation of the peak load.

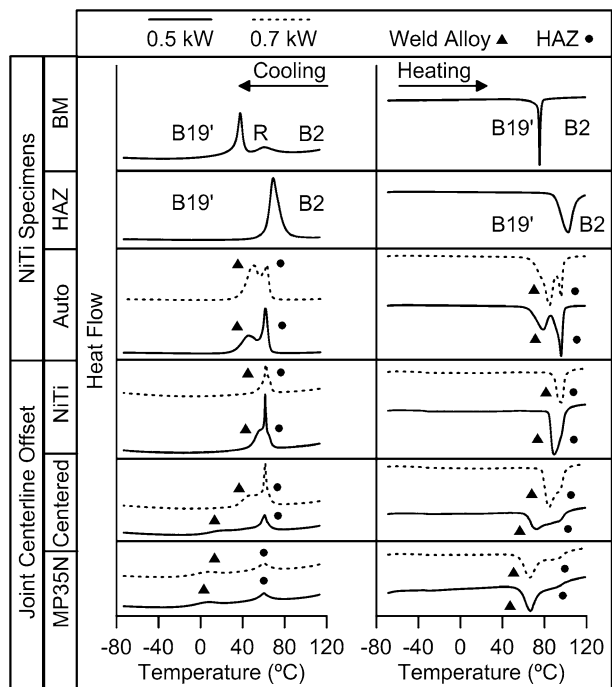


Fig. 12—DSC results of NiTi BM, Annealed (HAZ), Autogenous NiTi welds (Auto), and NiTi-MP35N offset welds (heat flow results not to scale).

annealed state (*i.e.*, simulated HAZ) as well as autogenous welds (Auto) performed on single wire NiTi material, were made to aid in the analysis of the dissimilar joints. The HAZ specimen was made by vacuum sealing NiTi BM in a quartz tube for a heat treatment at 1073 K (800 °C) for 1 hour in an air furnace, followed by a water quench.

The DSC trace of the BM in Figure 12 includes the R-phase transformation; typical of NiTi SMAs that have undergone cold-work and/or subsequent aging heat treatments to increase phase transformation temperatures and improve yield strength.^[20] The annealed BM has a higher transformation temperature, and no longer exhibits the R-phase transformation. Any Ti₂Ni intermetallics present will be in the form of Ti intermetallic oxides, which are considered inert inclusions.^[35] These inclusions will not be dissolved by a solutionizing heat treatment, and so do not affect the transformation temperature.^[35] The shift to higher temperatures, which was observed following the annealing heat treatment, is indicative of loss of cold work in the NiTi BM.^[38]

The NiTi autogenous laser welds have two sets of transformation peaks that were from the variation in properties between the FZ and HAZ.^[13] The low-temperature peak resulted from the weld metal, and the high-temperature peak has previously been shown to occur due to the effects of the HAZ in Ni-rich NiTi alloys.^[8,15] The HAZ has experienced solutionizing temperatures, which led to phase transformations at similar temperatures to that of the annealed BM peak due to the previously mentioned loss of cold work.^[13] The loss of cold work, indicated by this shift in transformation temperature, contributed to the failure through the weakened HAZ of the specimens. Because this was a Ti-rich alloy, the high-temperature peak may also include the R-phase transformation.^[15] The R-phase transformation in the FZ has been shown to occur because of the formation of Ti₂Ni precipitates along the grain boundaries, as reported by a previous pulsed Nd:YAG investigation of Ti-rich NiTi.^[15] Conflicting results have been reported when continuous Nd:YAG welding was used with Ti-rich NiTi.^[17] The continuous laser welding process would experience both minimal compositional change from evaporation, and a lower cooling rate in the FZ.^[8,17] The lower cooling rate and less Ti-rich composition can contribute to the favored formation of NiTi over Ti₂Ni in the FZ.^[39] The lack of Ti₂Ni would lead to no R-phase being observed in the DSC traces of the continuous welding investigation.^[17]

With a good understanding of the phase transformation characteristics of the NiTi BM, annealed NiTi, and autogenous NiTi weld, we can now examine the effects of welding the dissimilar NiTi wire to the MP35N wire. Phase transformation peaks resulting from the FZ, HAZ, and intermediate phase transformations were observed for each joining condition. The MP35N wire contains elements which are *M_s* depressants which would cause a decrease in transformation temperature if alloyed with NiTi.^[22] The compositional measurements were confirmed by the shift in transformation temperatures that occurred as more martensite transformation-stabilizing elements were introduced into the FZ. The NiTi offset welds were shown to be mostly NiTi, and so there was little change in the position of the transformation peak temperatures compared with autogenous welds. The centered joints experienced an intense amount of mixing which led to a decrease in the weld alloy's transformation temperatures.^[20–22] The MP35N offset joints have the lowest transformation

temperature because the FZs were dominated by the MP35N alloying elements.^[20,22] The joints welded with higher power have higher transformation temperatures in the weld region. It has been previously proven that the preferential evaporation of Ni instead of Ti during laser welding will lead to a more Ti-rich matrix, which will contribute to the observed increase in transformation temperatures.^[8,13]

The existence of multiple phases (*i.e.*, martensite and austenite) in contact with one another and the resultant mismatch in crystal structures are accompanied by an increase in stress at the interface.^[20] This may affect the properties of the specimen. The phases in the BM and FZ of the NiTi offset joint have similar transformation temperatures. This near homogeneity will limit any increase in stress and may have a limited effect on the material properties and fracture path. The MP35N offset FZ is austenitic at room temperature, while the BM is martensitic. This mismatch in phases will increase the stress at the interface and may have contributed to the fracture path along the FB. The effect of these coexistent phases would be of interest in future cyclic actuation and fatigue investigations.

IV. CONCLUSIONS

The laser welding of NiTi wire to MP35N wire was investigated to improve the understanding of dissimilar materials joining of NiTi SMAs and facilitate their future application in novel devices. The effects of varying the laser power, and the offset of the laser spot from the joint's centerline were studied. The main findings were as follows:

1. Laser offset from the joint's centerline was shown to affect the weld pool composition. This affected the mixing of Ti with the MP35N alloy, the hardness profile across the FZ, the amount of cracking, and the peak load of the tensile specimens. The MP35N offset joints had the lowest mixing of Ti in the FZ, and the lowest average hardness in the FZ, achieving the highest average peak load of 92 ± 4 N (66 pct of BM breaking load) with minimal defects.
2. The laser power affected the weld pool size, BM dilution, and the mixing of Ti with the MP35N alloy in the FZ. Joints made at lower powers had smaller FZs, with the less mixing of Ti, which resulted in a lower hardness and less cracking.
3. Using laser offset to control the MP35N content of the weld pool determines the reduction in M_S transformation of the NiTi. This alteration of the phase transformation properties is an important variable to consider when designing SMA devices that contain dissimilar joints.

ACKNOWLEDGMENTS

The authors would like to acknowledge the supports of the Natural Sciences and Engineering Research Council of Canada (www.nserc.ca), the Canada

Research Chairs Program (www.chairs-chaire.gc.ca), and the Ontario Centres of Excellence (<http://www.occ-ontario.org/>).

REFERENCES

1. D.J. Hartl and D.C. Lagoudas: *Proc. Inst. Mech. Eng. G* 2007, vol. 221 (4), pp. 535–52.
2. F. Butera: *Adv. Mater. Process.*, 2008, vol. 166 (3), pp. 37–40.
3. T. Duerig, A. Pelton, and D. Stockel: *Mater. Sci. Eng. A*, 1999, vols. A273–275, pp. 149–60.
4. P. Sevilla, F. Martorell, C. Libenson, J.A. Planell, and F.J. Gil: *J. Mater. Sci. Mater. Med.*, 2008, vol. 19, pp. 525–529.
5. Y. Fu, W. Huang, H. Du, X. Huang, J. Tan, and X. Gao: *Surf. Coat. Technol.*, 2001, vol. 145 (1–3), pp. 107–12.
6. A. Pequegnat, M. Daly, J. Wang, Y. Zhou, and M.I. Khan: *Smart Mater. Struct.*, 2012, vol. 21 (9), p. 094004.
7. A. Pequegnat, M. Daly, J. Wang, Y. Zhou, and M.I. Khan: *Smart Mater. Struct.*, 2012, vol. 21, art. id 094004.
8. M.I. Khan, A. Pequegnat, and Y. Zhou: *Adv. Eng. Mater.*, 2013, vol. 15 (5), pp. 386–93.
9. B. Tam, A. Pequegnat, M.I. Khan, and Y. Zhou: *Metall. Mater. Trans. A*, 2012, vol. 43A, pp. 2969–78.
10. S. Fukumoto, T. Inoue, S. Mizuno, K. Okita, T. Tomita, and A. Yamamoto: *Sci. Technol. Weld. Join.*, 2010, vol. 15 (2), pp. 124–30.
11. M.I. Khan, S.K. Panda, and Y. Zhou: *Mater. Trans.*, 2008, vol. 49 (11), pp. 2702–08.
12. P. Schlossmacher, T. Haas, and A. Schussler: *J. Phys. IV France*, 1997, vol. 7, pp. C5-251–C5-256.
13. B. Tam, M.I. Khan, and Y. Zhou: *Metall. Mater. Trans. A*, 2011, vol. 42A, pp. 2166–75.
14. P. Schlossmacher, T. Haas, and A. Schussler: *Proc. Conf. SMST-97*, 1997, pp. 137–42.
15. P. Schlossmacher, T. Haas, A. Schussler: *Proc. Conf. SMST International Conference*, 1994, pp. 85–90.
16. J. Pouquet, R.M. Miranda, L. Quintino, and S. Williams: *Int. J. Adv. Manuf. Technol.*, 2012, vol. 61, pp. 205–12.
17. A. Falvo, F.M. Furgiuele, and C. Maletta: *Mater. Sci. Eng. A*, 2005, vol. 412 (1–2), pp. 235–40.
18. M.I. Khan and Y. Zhou: *Mater. Sci. Eng. A*, 2010, vol. 527 (23), pp. 6235–38.
19. M.I. Khan and Y.N. Zhou: World Intellectual Property Organization (WIPO) Patent Application WO/2011/014962, 2011.
20. K. Otsuka and X. Ren: *Prog. Mater. Sci.*, 2005, vol. 50 (5), pp. 511–678.
21. M. Daly, A. Pequegnat, Y. Zhou, and M.I. Khan: *Smart Mater. Struct.*, 2012, vol. 21 (4), p. 045018.
22. T. Homa: in *Shape Memory Materials*, H. Funakubo, ed., Gordon and Breach Scientific Publishers, New York, 1987, p. 83.
23. H.M. Li, D.Q. Sun, X.L. Cai, P. Dong, and W.Q. Wang: *Mater. Des.*, 2012, vol. 39, pp. 285–93.
24. H. Li, D. Sun, X. Cai, P. Dong, and X. Gu: *Opt. Laser Technol.*, 2013, vol. 45, pp. 453–60.
25. R. Hahnen, G. Fox, and M.J. Dapino: *JIMSS*, 2012, 17pp.
26. J. Vannod, M. Bornert, J.-E. Bidaux, L. Bataillard, A. Karimi, J.-M. Drezet, M. Rappaz, and A. Hessler-Wyser: *Acta Mater.*, 2011, vol. 59 (17), pp. 6538–46.
27. Z. Song, K. Nakata, A. Wu, and J. Liao: *Mater. Sci. Eng. A*, 2013, vol. 560, pp. 111–20.
28. H.C. Chen, A.J. Pinkerton, and L. Li: *Int. J. Adv. Manuf. Technol.*, 2010, . DOI:10.1007/s00170-010-2791-3.
29. G. Satoh, Y.L. Yao, and C. Qiu: *Int. J. Adv. Manuf. Technol.*, 2012, . DOI:10.1007/s00170-012-4342-6.
30. Y.D. Huang, A. Pequegnat, J.C. Feng, M.I. Khan, and Y. Zhou: *Sci. Technol. Weld. Join.*, 2011, vol. 16 (7), pp. 648–56.
31. Y.D. Huang, A. Pequegnat, G.S. Zou, J.C. Feng, M.I. Khan, and Y. Zhou: *Metall. Mater. Trans. A*, 2012, vol. 43A, pp. 1234–43.
32. S. Kou: *Suppl. Weld. J.*, 2012, vol. 91, pp. 287–s–302-s.
33. Y.T. Hsu, Y.R. Wang, S.K. Wu, and C. Chen: *Metall. Mater. Trans. A*, 2001, vol. 32A, pp. 569–76.

34. N.J. Noolu, H.W. Kerr, Y. Zhou, and J. Xie: *Mater. Sci. Eng. A*, 2005, vol. 397 (1–2), pp. 8–15.
35. H.C. Lin, S.K. Wu, and J.C. Lin: *Mater. Chem. Phys.*, 1994, vol. 37, pp. 184–90.
36. D.M. Goldstein: United States Naval Ordinance Laboratory, White Oak, 1965, pp. 64–235.
37. S. Chatterjee, T. Abinandanan, and K. Chattopadhyay: *J. Mater. Sci.*, 2006, vol. 41 (3), pp. 643–52.
38. H.C. Lin, S.K. Wu, T.S. Chou, and H.P. Kao: *Acta Metall. Mater.*, 1991, vol. 39 (9), pp. 2069–80.
39. R. Nagarajan and K. Chattopadhyay: *Acta Metall Mater.*, 1994, vol. 42 (3), pp. 947–58.